Discovery of Novel Allosteric Sites of SARS-CoV-2 Papain-Like Protease (PLpro)

Juliana C. Ferreira[1], Kenana Al Adem[1], Samar Fadl[1], Adrian J. Villanueva[1], Lara Alzyoud[2,3], Mohammad A Ghattas[2,3] and Wael M. Rabeh[1, *]

1 Science Division, New York University Abu Dhabi, PO Box 129188, Abu Dhabi, United Arab Emirates.

2 College of Pharmacy, Al Ain University, Abu Dhabi 64141, United Arab Emirates

3 AAU Health and Biomedical Research Center, Al Ain University, Abu Dhabi 64141, United Arab Emirates

*Corresponding author: wael.rabeh@nyu.edu

Keywords: COVID-19, SARS-CoV-2, papain-like protease (PLpro), allosteric sites, thermodynamic stability, initial velocity studies.

Abstract (250 words)

Papain-like protease (PLpro) is a viral protease found in some coronaviruses, including SARS-CoV-2, the virus that causes COVID -19. Inhibition of PLpro activity could potentially limit viral replication, making it an attractive target for antiviral drug development. This work describes the discovery of novel allosteric residues of SARS-CoV-2 PLpro that can be targeted with antiviral drugs. First, a computational analysis was performed to identify potential druggable pockets on the surface of SARS-CoV-2 PLpro. The computational analysis predicted three druggable pockets around PLpro's surface and are located at the interfaces of its four domains. Pocket 1 is located at the interface between the Ub1 and thumb domains, pocket 2 is at the interface between the thumb, finger, and palm domains, and pocket 3 is at the interface between the finger and palm domains. Targeted alanine mutagenesis of selected residues with important structural interactions revealed 14 residues that are essential for maintaining a catalytically active and thermodynamically stable PLpro. Namely, these residues are T10, D12, T54, Y72, and Y83 in pocket 1; Q122, S239, Q237, H275, and S278 in pocket 2; and S212, Y213, Y251, K254, and Y305, in pocket 3. In addition to this, residues that were found important to catalysis were recovered by mutating them to amino acids of similar physicochemical properties to further elucidate the mechanistic properties of the local interactions they make. Experimental work confirms essential contacts are present in the allosteric sites of PLpro that could be targeted with non-competitive inhibitors as novel therapeutics against COVID -19.

Introduction

As the globe anticipates the subsidence of the reported number of new coronavirus disease 2019 (COVID-19) cases, scientists continue racing to develop more antivirals against severe acute respiratory syndrome-coronavirus 2 (SARS-CoV-2) to combat the impending threat of viral mutations and antiviral resistance. In the past three years, the world has witnessed sequential outbreaks of SARS-CoV-2 variants that resulted in waves of worldwide infection with symptoms that ranged between influenza-like symptoms and acute lower respiratory infections accompanied by dyspnea and pneumonia (Lan, Filler *et al.* 2020). Since its emergence in December 2019 in Wuhan, China, the World Health Organization (WHO) has reported more than 700 million cases and over 6 million deaths (Shetler, Ferreira *et al.* 2022, WHO 2022). SARS-CoV-2 is a single-stranded RNA virus having characteristic crown-like projections displayed on its surface (Wu, Wu *et al.* 2020, Chadha, Khullar *et al.* 2022), with the viral ability to encode for four different structural proteins, namely, Spike (S), Envelope (E), Membrane (M), and Nucleocapsid (N) proteins (Kaur and Gupta 2020).

The entry of SARS-CoV-2 into the host cell is initiated by the S protein when it binds to angiotensin -converting enzyme 2 (ACE2), the main host cell receptor, via the S1 subunit of the spike protein (Zhang, Xiang *et al.* 2021, Jackson, Farzan *et al.* 2022). Subsequently, SARS-CoV-2 begins entry into the cell through a membrane-fusion step via the S2 subunit of the spike protein (Li 2016). Upon entry into the cell, the viral genomic RNA is introduced into the host cell and is then translated into non-structural (nsps) polyproteins by means of two open reading frames (ORFs), ORF1a and ORF1b, that produce two polyproteins, pp1a and pp1ab, respectively (Kim, Lee *et al.* 2020, V'Kovski, Kratzel *et al.* 2021). PLpro is required for the proteolytic release of nsp 1-4, whereas 3CLpro is required for the proteolytic release of nsp 5 – 16 (Krichel, Falke *et al.* 2020, Wu, Chen *et al.* 2020).

Not only do nsps play a critical role in viral transcription and replication, but they also counteract the host innate immunity responses. Thus, the study of nsp assemblies and functions provides a foundation for the development of novel drugs targeting viral infections and immune evasion machinery (Rohaim, El Naggar *et al.* 2021, Shetler, Ferreira *et al.* 2022). Previous studies have shown that PLpro from various coronaviruses has an antagonistic ability to evade the innate immune system of the host and start viral replication. The mechanism involves the inhibition of the phosphorylation and nuclear translocation of the interferon regulatory factor-3 (IRF3) by PLpro polyprotein, resulting in deactivation of

the type I interferon (IFN) response (Chen, Yang *et al.* 2014). Moreover, the processes of ISGylation and ubiquitination are key elements in the activation of the innate immune response, which, if disrupted by a virus, would lead to successful viral infection. In fact, PLpro was reported to have deubiquitination properties (DUB) homologous to human deubiquitinases. This allows PLpro to cleave ubiquitin and ubiquitin-like modifiers such as interferon-stimulated gene 15 (ISG15), which is known to be induced during viral infections. Consequently, inflammation and antiviral signalling of the immune system are inhibited by PLpro domain. As a result, the host's ability to recognize and degrade the invading viral proteins is hindered (Yang, Chen *et al.* 2014, Klemm, Ebert *et al.* 2020). Thus, considering the structural and functional properties of PLpro would allow the development of antiviral drugs against various coronaviruses such as SARS-CoV-2, SARS-CoV, and MERS-CoV.

The tertiary structure of SARS-CoV-2 PLpro monomer adopts a right-handed conformation composed of two main domains, namely the ubiquitin-like (Ub1) domain and the catalytic domain (Ferreira, Pillaiyar *et al.* 2022). The N-terminal Ub1 domain of PLpro consists of residues 1 – 60, which form 5 β-strands, a single α-helix and a single 3_{10} helix. The catalytic domain is further divided into three main subdomains responsible for enzyme activity: Thumb, Finger, and Palm domains (Ferreira, Pillaiyar *et al.* 2022). The thumb domain (61 - 176) has 6 α-helices and two small β-strands, while the finger domain (177 - 238) contains the zinc binding site and consists of 5 β-strands and two α-helices. The palm domain spans residues 239 - 315 and consists of 6 β-strands. The catalytic site of PLpro is located between the thumb and palm subdomains and consists of three amino acids (Cys111, His272, and Asp286), known as the "catalytic triad", that are essential for the proteolytic mechanism of the enzyme (Baez-Santos, St John *et al.* 2015, Klemm, Ebert *et al.* 2020, Osipiuk, Azizi *et al.* 2021). The Ub1 domain binds ubiquitin or ISG15 in an "open hand" structure, with ubiquitin resting on the palm subdomain. The zinc-binding finger, consisting of four conserved cysteine residues (C189, C192, C224, and C226), holds the ubiquitin in place and is an essential component for the structural integrity and activity of the protease (Lv, Cano *et al.* 2021). Previous studies have shown that alanine substitution of the cysteine residues in the zinc-binding domain would result in complete loss of PLpro function (Barretto, Jukneliene *et al.* 2005), because them maintain the structural integrity of PLpro (Barretto, Jukneliene *et al.* 2006; Báez-Santos, St John *et al.* 2015, Esposito, D'Abrosca *et al.* 2022).

Due to the highly rapid and destructive proliferation of SARS-CoV-2 across the globe, the scientific community has witnessed the development of therapeutic drugs for COVID-19 treatment at an unprecedented rate. In the early stages of the COVID-19 pandemic, many research efforts have turned to drug-repurposing, a strategy that involves testing a collection of approved or investigational drugs against SARS-CoV-2 targets, like 3CLpro and PLpro (Pushpakom, Iorio *et al.* 2019, Cavasotto and Di Filippo 2021, Kandeel, Abdelrahman *et al.* 2021, Luo, Qiu *et al.* 2021). Owing to the immediate meteoric rise in the prevalence of COVID-19 in early 2020 and the urgency created along with it, a drug-repurposing strategy was viewed as a promising course of action, in hopes of accelerating the development of COVID-19 treatments. Numerous *in-silico* attempts have been made in repurposing drugs to target SARS-CoV-2 PLpro, but putative drug candidates still remain to be biochemically confirmed (Klemm, Ebert *et al.* 2020, Smith, Davis-Gardner *et al.* 2020, Redhead, Owen *et al.* 2021, Xu, Chen *et al.* 2021, Zhao, Du *et al.* 2021). Meanwhile, several repurposed drug candidates against PLpro have gained traction when tested in-vivo or in-vitro – Simeprivir, Tanshinone, Famotidine and Ebselen, to name a few (Jin, Du *et al.* 2020, Gammeltoft, Zhou *et al.* 2021, Lim, Tan *et al.* 2021, Mura, Preissner *et al.* 2021, Anson, Chapman, et al. 2020). However, these drug candidates are either found clinically ineffective, are still under clinical trials, or still require thorough biochemical assessment (Calleja, Lessene *et al.* 2022). Screening for novel small-molecule inhibitors against PLpro is an alternative, but costly and time-consuming, strategy (Amin, Ghosh *et al.* 2021, Quimque, Notarte *et al.* 2021, Gogoi, Borkotoky *et al.* 2022, Jiang, Yang *et al.* 2022). Upon identification of a drug lead, potential inhibitors are often subjected to further optimization and drug design to improve potency and selectivity (Shan, Liu *et al.* 2021, Weglarz-Tomczak, Tomczak *et al.* 2021). By screening a vast collection of molecules and carrying out further drug optimizations on lead molecules, inhibitors can reach a potency down to the nanomolar order of magnitude (Ma, Sacco *et al.* 2021, Shan, Liu *et al.* 2021). Lastly, zinc-ejecting drugs have also been shown to have inhibitory potential against PLpro. They are a class of inhibitors which aim at targeting the metalloenzymes that have a common zinc-finger motif, like that in PLpro. Several zinc-ejecting drugs have been approved by the Food and Drug Administration (FDA) and are currently on the market. The mechanism behind these drugs is to disrupt the zinc-cysteine tetrahedral complex by means of displacing the metal ion (Krishna, Majumdar et al. 2003, Gao, Qin et al. 2020, Shetler, Ferreira *et al.* 2022). However, there is an emerging debate regarding the efficacy of zinc-ejecting drugs; molecular dynamics studies on PLpro suggest that the labile zinc finger subdomain is a highly mobile region, making the zinc-finger

structural motif a poor drug target as it would prove challenging for small molecule drugs to bind to tightly (Bosken, Cholko *et al.* 2020). On the other hand, some studies have reported that zinc-ejecting drugs, such as ebselen and disulfiram, disrupt the stability of PLpro, thereby reducing its catalytic activity. These findings suggest the possibility of using zinc-ejecting drugs together with other antiviral drugs to treat COVID-19 symptoms in a so-called "multi-target approach" (Lin, Moses *et al.* 2018, Ma, Hu *et al.* 2020, Sargsyan, Lin *et al.* 2020, Calleja, Lessene *et al.* 2022).

Nonetheless, the world is still pressed for the development of an effective therapeutic agent against COVID-19. Out of the potential targets against SARS-CoV-2, PLpro remains to be an exceptional protein of interest as it plays a dual role in viral replication and evasion of the antiviral immune response. Herein, we identified three novel binding pockets in SARS-CoV-2 PLpro *in-silico.* Inside each of the identified binding pockets, selected amino acid residues with important structural interactions were biochemically and thermodynamically characterized *in-vitro* after site-directed mutagenesis. Mutagenesis studies were conducted to confirm the druggability of these identified binding pockets from our computational findings. This research study is aimed to aid the development of novel non-competitive drugs that can allosterically bind and inhibit PLpro and ultimately be used as a therapeutic drug in our efforts to combat the spread of COVID-19.

Materials and Methods

Selection and preparation of PLpro crystal structures

The Protein Data Bank was used to download all PLpro crystal structures used in this work (http://www.rcsb.org). All structures considered were solved using X-crystallography and contained no mutated residues; otherwise, they were discarded. Overall, 22 PLpro crystal structures were included in the analysis.

Each structure was then prepared by MOE (Molecular Operating Environment, 2021). The solvent atoms from each crystal structure were removed, and any missing atoms, residues, chains, or loops were added using the protein preparation module. Then, Protonate3D was used to assign each atom a unique protonation state. The prepared crystal structures were then imported into Maestro (Schrödinger, 2021), where the Protein Preparation wizard (Schrödinger, 2021) module is used to refine proteins to maintain structural integrity.

Hydrogens were added using hydrogen bond optimization, and the structures were then subjected to restrained minimization to achieve a reduced energy state.

Druggability Assessment of allosteric sites

The SiteMap (Schrödinger, 2021) module was used to process proteins, with all settings left at their default. To prevent any bias from utilizing ligands or peptides to identify pockets, the "Identify top-ranked possible receptor binding sites" option was used. SiteMap computes numerous physiochemical parameters for each site, such as size, exposure, hydrophobicity, hydrophilicity, and volume (Halgren, 2009). Most significantly, it assigns a Dscore to each protein binding pocket using a weighted equation:

$$\text{Dscore} = 0.094\sqrt{n}+0.60e-0.324p \qquad \text{(eq. 1)}$$

Where n denotes the number of site points, e denotes the enclosure factor, and p denotes the hydrophilicity.

Analyzing scores obtained by SiteMap

To analyze the Dscores produced by SiteMap (Schrödinger, 2021), Halgren (Halgren, 2009) proposed a classification system with a threshold to differentiate druggable sites from difficult sites. This approach can correctly predict the ligand binding site in 86% of protein-ligand complexes according to their Dscores. Sites are classified as difficult if their Dscore is less than 0.8, druggable if their Dscore is between 0.8 and 1.0, and very druggable if their Dscore is greater than 1.0.

Expression and purification of WT and PLpro mutants

The recombinant PLpro wild type and mutants' genes with an N-terminal Hisx6 tag was introduced into the pET-28b (+) bacterial expression vector by GenScript, Inc. (Piscataway, NJ). The vector was used to transform E. coli BL21-CodonPlus-RIL (Stratagene) for protein expression as described previously (Shetler, Ferreira *et al.* 2022). The inoculated culture (5 L) was grown at 30 °C in lysogeny broth (LB) with 100 mg/L kanamycin, 50 mg/L chloramphenicol, and 1 μM $ZnCl_2$ until OD_{600} = 0.5. The temperature was then reduced to 15 °C, and protein expression was induced overnight (14-16 h) by adding 1 mM IPTG. The cells were pelleted by centrifugation at 12,000 xg and 4 °C for 10 min in an Avanti J26-XPI centrifuge (Beckman Coulter Inc.). The cell pellets were homogenized in lysis buffer (25 mM Tris, 150 mM NaCl, 5 mM imidazole, 3 mM β-mercaptoethanol (βME), and 0.1% protein inhibitor cocktail (Sigma-Aldrich: P8849) before sonication on ice. The cell lysate was then

centrifuged at 40,000 xg and 4 °C for 45 min. The supernatant was loaded onto a nickel column pre-equilibrated with binding buffer (25 mM Tris, 150 mM NaCl, 5 mM imidazole, and 3 mM βME). The column was washed with binding buffer supplemented with 25 mM imidazole, followed by elution with binding buffer supplemented with 300 mM imidazole. The nickel column fractions containing PLpro were pooled and loaded onto a HiLoad Superdex 200 size-exclusion column (GE Healthcare) on an ÄKTA pure 25 chromatography system (Cytiva, USA). The gel filtration column was pre-equilibrated with 20 mM HEPES pH 7.5, 150 mM NaCl, and 0.5 mM tris(2-carboxyethyl)phosphine (TCEP). The PLpro-containing fractions were collected and concentrated to ~150 μM. The sample concentration and purity were determined by the Bradford assay and SDS-PAGE, respectively.

Enzyme titration and initial velocity studies

PLpro enzyme titration and initial velocity analyses were performed using a Cytation 5 multi-mode microplate reader (BIOTEK Instruments, Winooski, VT), as described previously (Shetler, Ferreira *et al*. 2022). The peptide substrate contained the PLpro cleavage site Leu-Arg-Gly-Gly flanked by a fluorescent AMC (7-amino-4-methyl coumarin) tag and corresponding quencher CBZ (carbobenzoxy) (*i.e.*, CBZ-LRGG-AMC). The proteolytic reaction was initiated by adding 0.5 μM PLpro enzyme to the peptide in buffer (50 mM HEPES pH 7.5, 0.5 mM EDTA, and 0.5 mM TCEP) containing 2% DMSO to enhance the solubility of the peptide (Shetler, Ferreira et al. 2022). The PLpro reaction was monitored in a 96-well microplate at 25 °C for 10 min at excitation and emission wavelengths of 340 nm and 487 nm, respectively. Cleavage of the peptide substrate by PLpro resulted in an increase in the AMC fluorescent signal.

To assess the effect of a single amino acid substitution on the rate of proteolysis by PLpro, the enzymatic activity of the WT enzyme and mutants was first assayed at different enzyme concentrations. The concentration of the peptide substrate was fixed at 200 μM, and the enzyme concentration was varied from 0.5 to 5 μM. Next, initial velocity studies were performed with the WT enzyme and the catalytically active mutants to determine K_m and k_{cat}. The concentration of the peptide substrate was varied from 20 to 800 μM at a fixed concentration of PLpro. The cleavage rate data were fit to the Michaelis–Menten equation using the global fitting analysis function in the kinetics module of SigmaPlot (Systat Software, Inc). Error bars were calculated from triplicate measurements of each reaction, and the results are presented as the mean ± SD.

Thermal Inactivation of PLpro WT and mutants

The thermal inactivation of PLpro variants was carried out by measuring the rates of enzyme sample incubated at 37 °C at different time intervals. The enzymatic activity of PLpro was determined as described above. Using Prism 9 (GraphPad Software), the decay in enzymatic activity was fitted to a one phase decay equation:

$$A = A_0 e^{-kt} \ (Eq.\ 2)$$

Where A is the relative activity of the enzyme at incubation time, t, A_0 is the activity of the enzyme at t=0, and k is the rate constant. The half-life ($t_{1/2}$) was defined to be the time at which enzymatic activity was reduced to half, which is equal to $\frac{ln\ (2)}{k}$.

Results

Structural assessment of putative binding sites on SARS-CoV-2 PLpro

PLpro is composed of 4 main domains: Ub1, thumb, finger and palm (Figure 1A). The secondary structural arrangements of the four PLpro domains result in a right-handed conformation of the monomeric unit of PLpro. Here, we used SiteMap module to identify potential druggable pockets on the surface of SARS-CoV-2 PLpro. SiteMap analysis revealed 5 top-ranked potential binding sites on PLpro that were assigned druggability scores based on their physiochemical parameters. Of the predicted pockets, the active site of PLpro and another small allosteric site located on the same side of the active site were assigned the highest druggability scores (**Figure S1**). On the other hand, three additional allosteric pockets, located at the opposite side of the active site have been identified with moderate druggability scores presumably due to their shallow nature (**Figure S1**). **Table 1** illustrates the distinctive physiochemical parameters of the predicted binding sites on PLpro surface. The small allosteric site, which received the highest ranking, has a large (n = 62 spheres), well-defined pocket (e = 0.67), with moderate hydrophilicity (p = 0.53). The other druggable pocket is the PLpro active site that has also shown a large (n = 75 spheres), slightly more defined (e = 0.68) cavity but with significantly higher hydrophilicity (p = 0.99). In addition, three other putative allosteric pockets have been identified on the PLpro surface with variable cavity sizes (**Table 1**). Pocket 1 resembles the small allosteric site in terms of its size (n = 61 spheres) and enclosure (e = 0.67), but due to its very high hydrophilicity (p = 1.02) its Dscore measures 0.74. Pockets 2 and 3, have smaller (n = 29 and 31 spheres, respectively), less

defined cavities (e = 0.58 and 0.62) and higher hydrophilicity (p = 0.89 and 0.99) with lower druggability scores (Dscore = 0.56 and 0.57), respectively.

The main objective of this study is to identify potential druggable pockets on SARS-CoV-2 PLpro surface that can allosterically regulate the enzyme activity. These allosteric pockets can be used as potential targets for the development of new drugs to combat COVID-19. The computational analysis described above predicted three potential allosteric pockets located at the opposite side of the PLpro active site. The three predicted pockets span different regions of PLpro and are located at the interface of its four domains including Ub1-thumb, thumb-palm and finger-palm domains as will be detailed below. The residues forming these three pockets are shown in **Table S1** and **Figure S1**.

Next, in Pockets 1-3, we identified key residues that were proposed to be important for PLpro activity due to their polar side chain interactions with other residues (**Figures 2-4**). The structural analysis we present below illustrates a network of possible intra-domain and inter-domain interactions between residues in each computationally-predicted allosteric pocket. Residues with side-chain interactions may have critical roles in maintaining the structural stability and catalytic activity of SARS-CoV-2 PLpro. Using site-directed mutagenesis, the selected residues are mutated to alanine and will be experimentally characterized to determine their effect on PLpro enzymatic activity and thermodynamic stability. Moreover, any alanine substitutions that resulted in a significant reduction in proteolytic activity will be 'rescued' by replacing the original amino acid with a residue having similar physicochemical properties. For instance, if D12A was found to be important in catalysis, D12 would be rescued by mutating it to glutamate or asparagine because it has similar physiochemical properties to aspartate. The resulting rescued mutants will be chemically and thermodynamically characterized. A total of 82 mutations (52 of which were alanine substitutions and 30 of which were rescue mutations) were purified and their proteolytic activities were measured and compared to the wild-type PLpro. Furthermore, the proteolytic activity of PLpro WT and the mutants was measured in a reaction buffer containing 20 mM HEPES pH 7.5, 100 mM NaCl, 1 mM TCEP, and 1 mM EDTA. Proteolytic activity was measured at varying enzyme concentrations (0.5 to 5.0 μM) in the presence of a constant peptide substrate concentration of 200 μM. The relative enzymatic activity of each mutant was calculated by comparing the slope of Relative rate vs. [Enzyme] plots for each mutant with that of WT. For the purpose of categorizing the identified residues based on their

importance in proteolytic activity, this study will define three boundaries: alanine mutants that showed relative proteolytic activity that is >60% are of no interest for further analysis; alanine mutants that showed relative proteolytic activity that is less than 60%, but greater than 15% will be considered to partially inactivate the protease; and alanine mutants that showed a relative proteolytic activity less than 15% will be considered significantly critical to the catalysis of PLpro. These categories will be color-coded accordingly when labeled in **Figures 2-4**.

Table 1. Mean values of druggability score (Dscore) and other SiteMap physiochemical parameters obtained from the 22 PLpro structures studied in this work.

Site	Dscore	Size	Enclosure	Hydrophilicity
Allosteric Site	0.97	62	0.67	0.53
Active Site	0.88	75	0.68	0.99
Pocket 1	0.74	61	0.67	1.20
Pocket 2	0.56	29	0.58	0.89
Pocket 3	0.57	31	0.62	0.99

Pocket 1: Interface between Ub1 and Thumb domains

Pocket 1 is located on the opposite side of the active site at the interface between the Ub1 (residues 1 - 60) and thumb (residues 61 - 176) domains and contains a network of intra-domain and inter-domain interactions (**Figure 2A-D**). Firstly, the side chain hydroxyl group of Y71 forms an intra-domain hydrogen bond with the side chain of D134 (2.7 Å) and an inter-domain hydrogen bond with the backbone of D12 (4.2 Å) (Figure 1A). Of these three residues, mutants D12A and Y71A reduced proteolytic activity to 8% and 48%, respectively (**Figure 2E**). D134A had no effect in proteolysis. Rescuing D12 and Y71 were found to recover proteolytic activity partially or completely. A partial recovery in activity was found in D12E, while a complete recovery in activity was found in D12N. Y71F and Y71T were found to completely recover and partially recover proteolytic activity, respectively. In addition to this cluster of interactions, Y72 forms an inter-domain hydrogen bond with the backbone of V11 (2.6 Å) (**Figure 2A**). Y72A showed little to no proteolytic activity (**Figure 2E)**. Interestingly, Y72T did not rescue proteolytic activity despite maintaining a polar hydroxyl side chain, while Y72F completely recovered proteolytic activity.

Moving to another region in Pocket 1, the side chain of D12 was also found to have 3 polar intra-domain interactions with the hydroxyl group of T10 (3.4 Å), the side chain of N15 (2.8 Å), and the backbone of N15 (2.7 Å) (**Figure 2B**). T10A displayed no proteolytic activity but N15A had no effect in catalysis compared to WT (**Figure 2E**). Additionally, E67 forms two polar inter-domain interactions with the imidazole moiety of H17 (3.4 Å) and the carboxamide moiety of N15 (4.4 Å) (**Figure 2B**). H17A and E67A slightly reduced enzymatic activity to 77% and 17%, respectively (**Figure 2E**).

In this third region in Pocket 1 (**Figure 2C**), K91 forms two polar interactions: an inter-domain interaction with D37 (4.6 Å) and an intra-domain interaction with N88 (2.9 Å). Alanine mutations on these residues showed little to no change in proteolysis (**Figure 2E**).

Finally, the amide group of N13 forms two intra-domain interactions with the hydroxyl groups of T54 (4.7 Å) and Y56 (4.2 Å) (**Figure 2D**). N13A did not affect proteolytic activity, T54A was inactive, and Y56A partially reduced proteolytic activity to 44% (**Figure 2E**). Attempts to rescue Y56 with tyrosine and phenylalanine partially recovered proteolytic activity. Being the only inter-domain interaction found in this cluster, the side chain of Y56 also forms a hydrogen bond with the side chain of Y83 (4.5 Å) (**Figure 2D**). Y83A was found to significantly reduce proteolytic activity to 12% (**Figure 2E**). Moreover, a set of intra-domain interactions were found in the Thumb domain between the side chain groups of E143, R138, N146 and Y83. The guanidine group of R138 forms a salt bridge with E143 (3.1 Å) and a hydrogen bond with N146 (3.4 Å). Lastly, N146 forms a short hydrogen bond with Y83 (2.6 Å) (**Figure 2D**). R138A, E143A, and N146A brought about minimal change in proteolysis (**Figure 2E**).

<u>Pocket 2: Interface between Thumb, Finger, and Palm domains</u>

Pocket 2 is a unique cavity as it found at the interface between three domains: Thumb (residues 61 - 176), Finger (residues 177 - 238), and Palm (residues 239 - 315) (**Figure 1B**). Firstly, at the interface of Thumb and Palm domains, the side chain groups of T115, T119 and Q122, form inter-domain interactions with the imidazole group of H275 with hydrogen bond distances of 3.0 Å, 3.6 Å, and 2.8 Å, respectively (**Figure 3A**). Of these four residues, mutating H275 to alanine led to a nearly inactive protease (**Figure 3E**). Q122A partially reduced proteolytic activity to 35%, while T115A had minimal change in protein activity. Rescuing Q122 with asparagine led to inactivity but rescuing with glutamate partially

recovered proteolytic activity to 52% (relative to WT). Most interestingly, however, T119A improved proteolytic activity by a significant amount, increasing it to 141% (relative to WT). This was the only alanine mutation found in this study to have significantly enhanced enzyme catalysis. The hydroxyl group of T277 forms an inter-domain hydrogen bond with Q122 (2.7 Å) and possibly an intra-domain interaction with the side chain of K279 (5.1 Å) (**Figure 3A**). T277A partially reduced proteolytic activity to 32% (**Figure 3E**). Rescuing T277 with serine rescued proteolytic activity to 81% (relative to WT). Lastly, another set of interactions were observed between H255, G256, S278 and K279 (**Figure 3A**). The backbone of K279 is within proximity to form hydrogen bond interactions with the side chain of S278 (3.7 Å) and the imidazole group of H255 (2.7 Å). The side chain of S278 also forms a hydrogen bond with the imidazole group of H255 (4.2 Å) and with the backbone of G256 (2.9 Å). H255A and S278A partially inactivated enzyme catalysis, reducing proteolytic activity to 43% and 16%, respectively (**Figure 3E**). K279A had no effect in catalysis. Despite the similar structural and chemical elements between serine and threonine, S278T surprisingly did not rescue enzymatic activity.

Moving to another region in Pocket 2, a cluster of notable polar interactions were also found at the interface between Thumb and Finger, (**Figure 3B**). The side chain of Q133 forms two intra-domain interactions with the side chain of K126 (3.5 Å) and the backbone of N128 (3.3 Å). Between these three residues, Only Q133A partially reduced proteolytic activity to 56% (**Figure 3E**). On the other hand, K126A and N128A had a small effect on proteolytic activity. Rescuing Q133 with asparagine did not rescue proteolytic activity but rescuing it with glutamate partially rescued enzyme activity to 88% (relative to WT). Moreover, the backbone of N177 forms an inter-domain interaction with the side chain of N128 (3.7 Å) and the side chain of N177 forms an intra-domain hydrogen bond with the side chain of D179 (3.7 Å) (**Figure 3B**). Only D179A partially inactivated the protease, reducing activity to 46% (**Figure 3E**).

Another region in Pocket 2 lies within the Thumb domain (**Figure 3C**). a set of short interactions were found between Q121, R140 and Y136; R140 forms a dual polar interaction with the hydroxyl group of Y136 (2.8 Å) and the backbone of Q121 (3.2 Å). R140A was found to partially reduce enzymatic activity (44%) (**Figure 3E**). In attempt to rescue proteolytic activity, R140K partially improved activity to 74% (relative to WT). Y136A was observed to have a small effect on proteolytic activity.

The last set of interactions found in pocket 2 lie in the interface between Finger and Palm. The side chain of Q237 forms an inter-domain interaction with the hydroxyl group of S239 (3.0 Å) (**Figure 3D**), both of which led to proteases with critically low activity when mutated to alanine (**Figure 3E**). A set of four amino acids (E238, Q236, S309, and T311) were found to form a network of short and, possibly, strong interactions (**Figure 3D**). The side chain of E238 forms a short inter-domain hydrogen bond with the side chain of Q236 (2.4 Å) and an inter-domain interaction with the hydroxyl group of S309 (3.3 Å). The side chain of Q236 was also found to form a short inter-domain interaction with the hydroxyl group of T311 (2.6 Å). Alanine mutants S309A and T311A presented a minimal effect on proteolytic activity (**Figure 3E**). On the other hand, Q236A and E236A was found to partially weaken catalysis, reducing relative enzymatic activity to 58% and 52%, respectively. Rescuing E238 with aspartate slightly improved activity. Meanwhile, E238Q had improved proteolytic activity to 71% (relative to WT).

<u>Pocket 3: Interface between Finger and Palm domains</u>

Pocket 3 is located at the interface between the Finger (residues 177 - 238) and Palm (residues 239 - 315) domains (**Figure 1A**). The side chain of K217 forms an intra-domain salt bridge with E214 side chain (3.2 Å) (**Figure 4B**). Alanine mutations on E214 and K217 partially reduced activity to 49% and 29%, respectively (**Figure 4A**). Moreover, the hydroxyl group of Y213 forms a short inter-domain interaction with the side chain of E307 (2.5 Å) (**Figure 4B**). In addition, the hydroxyl group of Y305 forms an inter-domain interaction with the backbone of Y213 (3.5 Å) and an intra-domain hydrogen bond with the side chain of Y251 (4.1 Å). Lastly, the side chain of Y251 is also predicted to form an inter-domain hydrogen bond with the hydroxyl group of S212 (4.4 Å). All alanine mutants of tyrosine residues (Y213A, Y251A, and Y305A) in this region resulted in complete inactivation of PLpro (**Figure 4A**). Y213T failed to rescue any proteolytic activity, while Y213F rescued proteolytic activity to 28% (relative to WT). Similarly, Y305T did not rescue any proteolytic activity, but Y213F slightly rescued proteolytic activity to only 6%. In sharp contrast, rescuing Y251 with phenylalanine and threonine both greatly improved proteolytic activity to 91% and 90%, respectively. S212A critically reduced enzymatic activity to 9%, while E307A partially reduced enzymatic activity to 29%. Interestingly, mutating S212 to threonine did not rescue proteolytic activity, but had completely inactivated it.

Another cluster of interactions are found in pocket 3 that are predominantly within the Palm domain, apart from a single inter-domain interaction with Q122 in the Thumb domain (**Figure 4C**). The side chain of K254 was found to simultaneously make two salt-bridges with the side chain groups of E295 (3.4 Å) and E252 (3.6 Å). Among these three residues, K254A was found to critically affect proteolysis, reducing enzyme activity to 9% (**Figure 4A**). Moreover, the hydroxyl group of T257 also forms an intra-domain hydrogen bond interaction with the backbone of K254 (2.6 Å), but T257A was found to have a minimal effect on proteolysis. Lastly, the side chain of K306 forms two interactions: one of which is an intra-domain interaction with T259 side chain (4.3 Å) and the latter is an inter-domain interaction with Q122 side chain (4.2 Å) (**Figure 4C**). Q122A, T259A, and K306A partially inactivated proteolytic activity. T259A and K306A reduced enzymatic activity to 44% and 53%, respectively (**Figure 4A**). The effects of Q122A on proteolysis was reported previously (**Figure 3E**).

Initial velocity studies of PLpro mutants at the three predicted allosteric pockets

Initial velocity studies were performed to obtain the kinetic parameters – turnover number (k_{cat}), Michaelis constant (K_m) and the catalytic efficiency (k_{cat}/K_m) – of PLpro mutants from the three predicted allosteric pockets (**Figure 5**). Initial velocity studies were only performed on partially active PLpro mutants, mutants that significantly enhanced proteolysis, and recovery mutants. Inactive PLpro mutants could not be studied for their effects on kinetic parameters of the enzyme. Generally, k_{cat} measurements for the chosen constructs followed similar patterns to that obtained from the enzyme titration analysis. Most K_m measurements in PLpro mutants revealed a lower affinity to the substrate, with a few exceptions in which no change in or higher affinity to the substrate was observed. Lastly, most of the PLpro variants revealed a lower catalytic efficiency than WT, while a few variants had a similar catalytic efficiency to WT.

Pocket 1:

D12A and Y71A of UB1 and Thumb, respectively, decreased k_{cat} compared to WT (**Figure S4**). A reduction in k_{cat} was observed by 10-fold for D12A. However, relative to D12A, rescued mutants of D12 (D12E and D12N) measured a higher k_{cat}. D12A had similar substrate affinity to WT. However, rescued mutants, D12E and D12N, increased in substrate affinity by almost 2-fold. Overall, all D12 mutants were observed to have a much lower catalytic efficiency than WT (**Figure 5A**). A reduction in k_{cat} was also observed by 2-fold for

Y71A. Y71F had a slightly higher k_{cat} than that of Y71A, while Y71T had a slightly lower k_{cat} than that of Y71A. Interestingly, Y71A, a mutant that reduced catalytic activity, had a smaller K_m than that of WT by almost 2-fold. In stark contrast, Y71F and Y71T measured a higher K_m by 3-fold and 2-fold, respectively. As a result of Y71A's low K_m, Y71A measured similar catalytic efficiency to WT. On the other hand, Y71F and Y71T both reduced catalytic efficiency by 6-fold. Rescued mutants, Y72F and Y72T, had a reduction in k_{cat} by 2-fold and 24-fold, respectively. Both Y72F and Y72T also had an increase in K_m by 2-fold. Resultingly, Y72F and Y72T had much lower catalytic efficiencies than that of WT, reducing k_{cat}/K_m by 5-fold and 40-fold.

Relative to WT, H17A was found to reduce k_{cat} by almost 2-fold and slightly reduced K_m, thus having a slightly lower catalytic efficiency. Similar to H17A, K91A also followed similar findings. K91A measured a lower k_{cat}, slightly higher substrate affinity, and thus had a slightly lower catalytic efficiency than WT. E67A was found to have significantly lower k_{cat} reducing it by almost 7-fold and had a higher K_m. Resultingly, E67A had a 9-fold decrease in catalytic efficiency.

Y56A was found to reduce k_{cat} by almost 3-fold. Relative to Y56A, its corresponding rescued mutants measured an increase in k_{cat}. All Y56 variants measured an increase in K_m, with Y56A having the lowest increase and Y56T having the largest increase. As a result, all Y56 variants had much lower catalytic efficiencies. Y83A had a significantly reduced k_{cat} (9-fold), a slightly reduced K_m, and overall a significantly low catalytic efficiency. While Y83F and Y83T improved k_{cat}, relative to Y56A, K_m increased by approximately 2-fold. Ultimately, rescued mutants of Y83 also had a significantly low catalytic efficiency, like that of Y83A. Other mutants in pocket 1 showed no significant differences compared to WT.

Pocket 2:

T119A, the only alanine mutant to have significantly improved enzymatic activity, had an increase in k_{cat} and K_m by 1.5-fold (**Figure S5**). Overall, T119A had similar catalytic efficiency to that of WT. Pocket 2 alanine mutants, Q122A, T277A, and S278A, decreased k_{cat} by 3-fold, K_m by 1.4-fold, and k_{cat}/K_m by 60% compared with WT (**Figure 5B**). Interestingly, rescuing Q122 with glutamate led to an increase in K_m by 2-fold and, by extension, a significant decrease in catalytic efficiency. Rescuing S278 with threonine measured a significantly low k_{cat} value, a 2-fold increase in K_m and thus a 60-fold decrease in catalytic efficiency. H255A also measured a decrease in k_{cat} (4-fold) and a slight increase in

K_m. Consequently, H255A led to a 6-fold decrease in k_{cat}/K_m. K279A showed a slightly lower k_{cat} than WT, but K_m remained the same.

Mutants Q133A, N177A, Y136A, R140A, and E238A decreased k_{cat} by 1.6-fold, with similar K_m values to WT, except for Q133A, Y136A, and E238A, which increased K_m by 1.1-fold, 1.2-fold and 1.5-fold, respectively (**Figure S5**). Rescue mutant Q133N reduced k_{cat} by 3-fold and increased K_m by 2-fold, consequently reducing catalytic efficiency by approximately 7-fold. Rescuing E238 with aspartate and glutamine showed no significant differences in kinetic parameters, in relation to E238A. Q236A was shown to have approximately a 4-fold decrease in k_{cat} and a 1.4-fold increase in K_m, yielding a significantly low k_{cat}/K_m (**Figure 5B**). Lastly, S239A showed a significant decrease in k_{cat} and a slight increase in K_m.

Pocket 3:

Nearly all mutants tested in Pocket 3 led to a significant decrease in catalytic efficiency (<50%) relative to the WT. In extreme cases, some mutants even reduced catalytic efficiencies to nearly zero (**Figure 5C**). In good agreement with enzyme titration analysis, S212A and S212T follow the same pattern in k_{cat}, but an approximate 3-fold increase in K_m is observed in S212T (**Figure S6**). While Y213F was shown to slightly recover proteolytic activity, an approximate 2-fold increase in K_m can be observed from the kinetic study. E214A was observed to reduce k_{cat} by half and double in K_m. Of the Y251 mutants, Y251T showed a reduction in k_{cat} by half. Otherwise, other Y251 mutants measured a k_{cat} that was nearly zero. All K_m measurements of Y251 mutants led to a slight increase. Both rescue mutants of Y305 led to a significantly low k_{cat} and a 2-fold or 3-fold increase in K_m. E307A measured a reduction in k_{cat} by 4-fold and no significant change in K_m.

Of all the mutants in Pocket 3, E252A yielded the highest k_{cat} (~80% of WT) and no change in K_m was observed. K254A, T259A, K306A, and K306R led to varying reductions in k_{cat}: 11-fold, 4-fold, 2-fold, and 3-fold, respectively. Additionally, amongst these mutants, a change in K_m was only observed in K306R (2-fold increase).

Thermal Inactivation of PLpro WT and mutants

Thermal inactivation studies were performed on PLpro WT and mutants to elucidate the relationship between stability and catalytic activity (**Figure 6**). PLpro variants were thermally inactivated by incubating enzyme samples in 37 °C and measuring the residual enzymatic activity of enzyme variants at different time points. The incubation was carried out for two

hours. PLpro variants that were found to critically inhibit proteolysis in our titration experiments (**Figure 2-4**) were not included in this experiment. The half-life ($t_{1/2}$) was defined to be the time at which 50% relative activity was attained and was used as a quantitative measure of the kinetic stability of the PLpro variants. All half-life measurements of the PLpro mutants were analyzed in relation to WT. Most PLpro mutants in pocket 1 were observed to have minimal effects on half-life (**Figure 6A – C**). More notably, however, the half-life of K91A and Y71A mutants was found to be approximately twice that of WT. Moreover, Y56A and E67A had a 50% increase in $t_{1/2}$ relative to WT. Meanwhile, PLpro mutants in pocket 2 were found to be more kinetically unstable (**Figure 6D – F**). N177A and E238A mutants decreased the half-life by 20% while T277A decreased half-life by 40%. Most importantly, Q122A and S278A mutants were found to have the fastest half-lives amongst all PLpro mutants tested here, decreasing its $t_{1/2}$ to almost 90%. Q133A, R140A, D179A, Q236A and H255A mutants were observed to have a 15 – 40% higher half-life than that of WT. Y136A had a similar $t_{1/2}$ to WT. Lastly, PLpro mutants in pocket 3 have generally low half-lives, apart from K306A that had a 50% increase in $t_{1/2}$ (**Figure 6G – I**). Alanine mutations on S212, K217, E252, K254, and T259 reduced $t_{1/2}$ of the WT PLpro by 30 – 50%. E307A had a similar $t_{1/2}$ to WT.

Discussion

In the fight against COVID-19 and the spread of SARS-CoV-2, the discovery of antiviral drugs and the development of therapeutics are of great importance. A conserved step in the maturation of coronaviruses is the processing of viral polyproteins to produce new viral particles (Pushpakom, Iorio *et al.* 2019, Cavasotto and Di Filippo 2021, Kandeel, Abdelrahman *et al.* 2021, Luo, Qiu *et al.* 2021). In addition to the main protease of SARS-CoV-2, PLpro is responsible for processing viral polyproteins and releasing functional proteins during viral infection, making it an attractive target for the development of antiviral therapeutics against COVID-19 (Krichel, Falke *et al.* 2020, Wu, Chen *et al.* 2020). Also, PLpro has been reported to have deubiquitinating (DUB) and deISGylating activities that inhibit the host innate immunity responses (Ratia, Kilianski *et al.* 2014, McClain and Vabret 2020). In this study, we present a novel computational and biochemical approach in discovering allosteric sites around the surface of an enzyme: three potential allosteric sites on the PLpro surface (**Figure S1**) were computationally identified and targeted for mutagenesis to biochemically assess their role in protease activity. Identification of important amino acid contacts in PLpro will aid in screening and developing antiviral drugs against COVID-19 and

related coronaviruses diseases. Additionally, mutating important residues with other residues of similar physicochemical properties gives us a deeper insight into the polar, and sometimes non-polar, interactions they make. It is also important to note that our approach in this study can be applied to other attractive protein targets. Herein, we present multiple residues in three allosteric sites that can significantly hinder proteolysis. These allosteric sites are located at the opposite side of the PLpro active site.

Pocket 1

Alanine mutations in Pocket 1, an allosteric site found between two domains: Thumb and UB1, led to multiple partial or complete inactivations of protease activity. In summary, Y56A, E67A, and Y71A led to a partial inactivation of the protease, which was measured to have less than 60% of enzyme activity relative to WT. Additionally, T10A, D12A, T54A, Y72A, and Y83A led to a drastic reduction in proteolytic activity.

In contrast to D134A that had no effect on PLpro activity, Y71A decreased PLpro activity by ~50%. This is evidence showing that Y71 only makes important interactions with the backbone of D12, despite having a closer contact with D134. Additionally, $t_{1/2}$ of Y71A increased by 2-fold compared to WT, which suggests that Y71A adopts a more robust conformational fold but has hijacked the activity of the protease. Rescuing Y71 with phenylalanine or threonine resulted in full or partial recovery of PLpro activity, which indicates the importance of both hydrophobic and polar interactions formed by the side chain of Y71 to maintain a functional structural fold of PLpro. Y72A inactivated PLpro proteolysis, while Y72F fully recovered proteolysis. This shows that the hydroxyl group in Y72 plays a trivial role in the structural fold of PLpro. Instead, simply the large aromatic ring of tyrosine maintains important local hydrophobic interactions to ensure a proper fold. This claim is further supported by Y72T activity: maintaining a hydroxyl group, but effectively reducing the residue's size, hardly recovered any proteolytic activity.

Aside from interacting with Y71, the side chain of D12 also makes several close hydrogen bond interactions with N15 and T10 (2.7 Å – 3.4 Å), making it well-placed (**Figure 2B**). Alanine mutations of D12 and T10 showed little to no proteolytic activity, which further highlights the importance of the interaction between D12 and T10. Interestingly, rescuing D12 with glutamate partially recovered proteolytic activity, but rescuing D12 with asparagine fully recovered proteolytic activity. Enzyme kinetics and titration analyses show that a longer side-chain, glutamate, is too large to take the place of D12 and effectively disrupts its

interactions with T10 and N15. On the other hand, asparagine is a perfect replacement to D12 as it maintains the correct side-chain length and its polar group still allows it to make close polar interactions with T10 and N15. Despite N15 having close contacts with D12 and E67, N15A surprisingly had no effect in proteolytic activity, which shows that it is unimportant in maintaining structural fold. Conversely, E67A led to a notable reduction in PLpro activity and H17A led to a slight decrease in proteolytic activity, suggesting the significance of its local inter-domain interactions with H17 in the structural fold of PLpro.

Our results further highlight the importance of inter-domain interactions in maintaining PLpro activity as evident by the interaction of Y83 (Thumb) with Y56 (Ub1) (**Figure 2D**). Y83A variant decreased PLpro activity by 90% and Y56A variant reduced the proteolytic activity by ~50%. Attempting to rescue Y56 with phenylalanine and threonine both partially recovered proteolysis. Like in the case of Y71, Y56 places a dual importance in creating local hydrophobic and polar interactions, as shown when mutated to a similarly-shaped nonpolar residue (phenylalanine) or a small, but polar, residue (threonine). Rescuing Y83 with phenylalanine was only found to properly rescue proteolysis. Much like the case of Y72, Y83 also places heavy emphasis on creating local hydrophobic interactions to ensure proper folding and catalysis, but not polar interactions. T54A was also found to completely inactivate PLpro. Interestingly, the side chain of T54 was found to only establish a single inter-domain polar interaction with N13. While the reason for which T54A inactivates PLpro, but not N13A, remains unknown, we hypothesize that T54 coordinates with a water molecule to maintain the stability of an important structural characteristic of the protease.

<u>Pocket 2</u>

Pocket 2 is a unique site located at the interface of three domains: Palm, Thumb, and Finger. In pocket 2, the mutants Q122A, Q133A, R140A, D179A, Q236A, E238A, H255A, T277A and S278A partially inactivated PLpro activity to less than 60% compared to WT. Meanwhile three variants Q237A, S239A and H275A led to a drastic reduction in PLpro activity.

H275A inactivated PLpro activity, which shows that H275 is most important in forming three close inter-domain polar interactions with Q122, T119, and T115. Conversely, alanine mutations on T119 and T115 showed insignificant change in proteolysis while Q122A mutant reduced PLpro activity by more than 60% as compared to WT, suggesting the importance of the inter-domain interaction between H275 and Q122. In addition, enzyme titration results suggests that T277 only forms an interaction with Q122 as both T277A and Q122A, but not

K279A, reduced PLpro enzymatic activity. Interestingly, rescuing Q122 with asparagine completely inactivated the protease. This may be attributed to asparagine having a shorter side chain than glutamine or glutamate. Consequently, when Q122 is mutated to asparagine, the distances of hydrogen bonding made originally by Q122 with T277 and H275 is lengthened, and thus the strength of these interactions is also weakened, disrupting the overall fold and enzymatic capabilities of the protein. This is further evidenced by the partial recovery observed in Q122E. T277S was successful in partially recovering proteolytic activity, which confirms its relevance in maintaining polar interactions with its hydroxyl group to Q122. Lastly, within the network of intra-domain interactions formed between K279, S278, H255 and G256, only the mutants S278A and H255A partially inactivated the enzyme, which shows that the only significant interaction is made between S278 and H255. S278T did not recover proteolysis, which may be attributed to the slightly bulkier nature of threonine, relative to serine, which could cause greater strain in the overall fold of the protease.

Enzyme titration analysis also confirms that Q133 simultaneously forms interactions with N128 and K126, as shown by a partial inactivation in proteolysis in Q133A and a slight decrease in activity in both N138A and K126A. Similar to the case of Q122, rescuing Q133 with glutamate, but not asparagine, recovered proteolysis. This shows that it is important for Q133 to maintain a sufficient side-chain length to make polar contacts with N128 and K126. Enzyme titration analysis also shows that the side-chain interaction of N177 with D179, not with N128, is important for maintaining PLpro activity.

The side-chain interactions of R140 with Q121 and Y136 are also important for enzyme activity with R140A reducing proteolysis to 44%. R140K was successful in recovering proteolytic activity, indicating the importance of having a basic side-chain to mediate the interactions between Q121, Y136 and R140.

The inter-domain interaction between Q237 and S239 is highly important to enzyme activity as substitutions of both residues by alanine resulted in complete inactivation of the enzyme. In addition, among the local network of interactions made by Q236, E238, S309 and T311, the inter-domain interactions of Q236 with T311 and E238 with S309 are also minimally important, while the intra-domain interaction of Q236 and E238 is more important as both Q236A and E238A partially inactivated the enzyme. Similar to Q122 and Q133,

maintenance of side-chain length is also important for E238, as E238Q promotes higher proteolytic recovery than E238D.

In addition, S122A and S278A had a much lower $t_{1/2}$ than the WT. This indicates that K279 and S278 are of particular importance as the corresponding alanine mutants thermally destabilizes the enzyme and disrupts proteolysis. Interestingly, most mutations introduced in pocket 2 resulted in higher affinity to the substrate. However, a general decrease in catalytic efficiency is observed because of a decrease in K_{cat} amongst pocket 2 mutants.

Pocket 3

Of the three pockets discussed in this study, Pocket 3 was found to have the most residues that drastically affect the activity and stability of the enzyme. In summary, alanine mutants, E214A, K217A, T259A, K306A, and E307A led to a partial inactivation (<60% relative enzymatic activity) in proteolytic activity. Meanwhile, S212A, Y213A, Y251A, K254A, and Y305A led to a drastic decrease in catalysis.

Based on the enzyme titration results, the inter-domain interaction of Y213 with E307 is crucial for maintaining a functional fold of the enzyme. Rescuing Y213 with phenylalanine, but not threonine, led to partial proteolytic recovery. The loss of a hydroxyl group in Y213 led to a sharp decrease in relative proteolytic activity, as indicated by the enzyme titration results in Y213F. The evidence described above highlights the importance of both hydrophobic and polar interactions formed by the side chain of Y213. Similar to Y213, the inter-domain and intra-domain interactions of Y305 with Y213 and Y251, respectively, are crucial. Interestingly, while both attempts to recover enzymatic activity of Y305A with phenylalanine and threonine were not successful, both replacements led to nearly full recovery of activity in the case of Y251. These results indicate the high specificity of the required chemical properties of Y305 with respect to the large hydrophobic aromatic ring and the hydroxyl group that allows for interactions with Y213 and Y251. Alanine mutation on S212 also had a drastic and negative effect on proteolysis, which indicates the significance of the inter-domain interaction formed by Y251 and S212 for enzymatic function. Interestingly, attempts to rescue S212 with threonine failed to restore enzymatic activity. This can be explained by threonine's slightly bulkier nature than serine. This suggests that keeping a small side chain in S212 is also important in the fold of the protease. S212A also has a half-life that is almost 3-fold less than that of WT and has reduced the catalytic efficiency of the enzyme by ~10-fold, which further highlights its significance in the stability and fold of the

protein. Moreover, enzyme titration analysis on K217 and E214 confirms the importance of their side chain interactions.

The alanine mutant of K254 drastically reduced the activity and the catalytic efficiency of the enzyme (~90%) and the attempt to rescue its activity with arginine substitution led to enzymatic recovery. Additionally, a slight decrease in activity is observed in E295 and E252. This suggests that these three residues form a small important network of interactions that is primarily mediated by K254. Enzyme titration results of K254R also indicates the importance of having a basic side chain to mediate this network of interactions.

Lastly, the two inter-domain and intra-domain interactions of K306 with Q122 and T259, respectively, are enzymatically important with alanine mutants of K306 and T259 resulting in ≤50% decrease in enzymatic activity and catalytic efficiency.

While attempts to recover important residues in these pockets resulted in partial or full recovery of proteolysis, kinetic analysis revealed that they also increased in K_m. The resulting decrease in substrate affinity in recovery mutants can be explained by slight changes in conformation that led to partial obstruction of the entry to the active site by the substrate. It is important to note that our study only investigates the effects of single-point mutations in these pockets. Herein, we identified several single-point mutations that led to the complete inactivation of the protease. We suspect that developing a small-molecule drug that can disrupt multiple vital residues from these pockets would make for an even more potent inhibitor. It is well documented that PLpro displays deubiquitinating activity (Ratia, Kilianski *et al.* 2014, McClain and Vabret 2020). Our study does not investigate the effects of disrupting these allosteric sites on deubiquitination. It is likely that deubiquitination will also be severely hindered but the extent to which deubiquitination is affected is largely unknown.

In conclusion, enzyme titration experiments, kinetic studies, and determination of enzyme half-life suggests that there are several residues that are attractive for drug targeting as they either drastically reduce the protease's activity or stability (or both). Namely, these residues are T10, D12, T54, Y72, and Y83 in pocket 1; Q122, S239, Q237, H275, and S278 in pocket 2; and S212, Y213, Y251, K254, and Y305, in pocket 3. These pockets were identified by scanning the surface of the PLpro protein and they are located at the interface between protein domains. These findings support the notion that inter-domain interactions are more likely to contribute to enzyme stability and activity as compared with intra-domain interactions. The importance of the allosteric residues in pocket 2 and pocket 3 has not been

experimentally examined in previous studies, as only a few molecular docking and molecular dynamics studies have examined the binding modes of some potential inhibitors against PLpro. Q122, R140 and K279 have been expected to interact with anti-viral compounds, Indinavir and Lopinavir, through hydrogen-bonding interactions (Shiwani Rana 2021, Elfiky 2022). Another study on computational drug design predicted several residues of PLpro, K217, E252, T257, T259, S278, Y305 and K306 to be involved with bonded interactions with 3 potential drugs (Raj 2021).

References

Amin, S. A., K. Ghosh, S. Gayen and T. Jha (2021). "Chemical-informatics approach to COVID-19 drug discovery: Monte Carlo based QSAR, virtual screening and molecular docking study of some in-house molecules as papain-like protease (PLpro) inhibitors." J Biomol Struct Dyn 39(13): 4764-4773.

Anson, B. J., Chapman, M. E., Lendy, E. K., Pshenychny, S., D'Aquila, R.T., Satchell, K.J.F. and Mesecar, A.D.. (2020). "Broad-spectrum inhibition of coronavirus main and papain-like proteases by HCV drugs" , 01 May 2020, PREPRINT (Version 1) available at Research Square [https://doi.org/10.21203/rs.3.rs-26344/v1]

Baez-Santos, Y. M., S. E. St John and A. D. Mesecar (2015). "The SARS-coronavirus papain-like protease: Structure, function and inhibition by designed antiviral compounds." Antiviral Research 115: 21-38.

Barretto, N., D. Jukneliene, K. Ratia, Z. Chen, A. D. Mesecar and S. C. Baker (2005). "The papain-like protease of severe acute respiratory syndrome coronavirus has deubiquitinating activity." J Virol 79(24): 15189-15198.

Barretto N, Jukneliene D, Ratia K, Chen Z, Mesecar AD, Baker SC. Deubiquitinating activity of the SARS-CoV papain-like protease. Adv Exp Med Biol. 2006;581:37-41. doi: 10.1007/978-0-387-33012-9_5. PMID: 17037501; PMCID: PMC7124015.

Bosken, Y. K., T. Cholko, Y. C. Lou, K. P. Wu and C. A. Chang (2020). "Insights Into Dynamics of Inhibitor and Ubiquitin-Like Protein Binding in SARS-CoV-2 Papain-Like Protease." Front Mol Biosci 7: 174.

Calleja, D. J., G. Lessene and D. Komander (2022). "Inhibitors of SARS-CoV-2 PLpro." Front Chem 10: 876212.

Cavasotto, C. N. and J. I. Di Filippo (2021). "In silico Drug Repurposing for COVID-19: Targeting SARS-CoV-2 Proteins through Docking and Consensus Ranking." Mol Inform 40(1): e2000115.

Chadha, J., L. Khullar and N. Mittal (2022). "Facing the wrath of enigmatic mutations: a review on the emergence of severe acute respiratory syndrome coronavirus 2 variants amid coronavirus disease-19 pandemic." Environ Microbiol 24(6): 2615-2629.

Chen, X., X. Yang, Y. Zheng, Y. Yang, Y. Xing and Z. Chen (2014). "SARS coronavirus papain-like protease inhibits the type I interferon signaling pathway through interaction with the STING-TRAF3-TBK1 complex." Protein Cell 5(5): 369-381.

Elfiky, A. A. (2022). "SARS-CoV-2 Papain-like Protease as a Target for Anti-HCV and Anti-HIV Proteases: In silico Perspective." Systematic Reviews in Pharmacy 13(4).

Esposito S, D'Abrosca G, Antolak A, Pedone PV, Isernia C, Malgieri G. Host and Viral Zinc-Finger Proteins in COVID-19. Int J Mol Sci. 2022 Mar 28;23(7):3711. doi: (Esposito S 2022). PMID: 35409070; PMCID: PMC8998646

Ferreira, G. M., T. Pillaiyar, M. H. Hirata, A. Poso and T. Kronenberger (2022). "Inhibitor induced conformational changes in SARS-COV-2 papain-like protease." Sci Rep 12(1): 11585.

Ferreira, J. C., S. Fadl, M. Ilter, H. Pekel, R. Rezgui, O. Sensoy and W. M. Rabeh (2021). "Dimethyl sulfoxide reduces the stability but enhances catalytic activity of the main SARS-CoV-2 protease 3CLpro." Faseb Journal 35(8).

Gammeltoft, K. A., Y. Zhou, C. R. Duarte Hernandez, A. Galli, A. Offersgaard, R. Costa, L. V. Pham, U. Fahnøe, S. Feng, T. K. H. Scheel, S. Ramirez, J. Bukh and J. M. Gottwein (2021). "Hepatitis C Virus Protease Inhibitors Show Differential Efficacy and Interactions with Remdesivir for Treatment of SARS-CoV-2 In Vitro." Antimicrob Agents Chemother 65(9): e0268020.

Gao X, Qin B, Chen P, Zhu K, Hou P, Wojdyla JA, Wang M, Cui S. Crystal structure of SARS-CoV-2 papain-like protease. Acta Pharm Sin B. 2021 Jan;11(1):237-245. doi: 10.1016/j.apsb.2020.08.014. Epub 2020 Sep 2. PMID: 32895623; PMCID: PMC7467110.

Gogoi, M., M. Borkotoky, S. Borchetia, P. Chowdhury, S. Mahanta and A. K. Barooah (2022). "Black tea bioactives as inhibitors of multiple targets of SARS-CoV-2 (3CLpro, PLpro and RdRp): a virtual screening and molecular dynamic simulation study." J Biomol Struct Dyn 40(15): 7143-7166.

Halgren, T. A. Identifying and Characterizing Binding Sites and Assessing Druggability. J. Chem. Inf. Model., 2009, 49 (2), 377–389. https://doi.org/10.1021/ci800324m.

Jackson, C. B., M. Farzan, B. Chen and H. Choe (2022). "Mechanisms of SARS-CoV-2 entry into cells." Nat Rev Mol Cell Biol 23(1): 3-20.

Jiang, H., P. Yang and J. Zhang (2022). "Potential Inhibitors Targeting Papain-Like Protease of SARS-CoV-2: Two Birds With One Stone." Front Chem 10: 822785.

Jin, Z., X. Du, Y. Xu, Y. Deng, M. Liu, Y. Zhao, B. Zhang, X. Li, L. Zhang, C. Peng, Y. Duan, J. Yu, L. Wang, K. Yang, F. Liu, R. Jiang, X. Yang, T. You, X. Liu, X. Yang, F. Bai, H. Liu, X. Liu, L. W. Guddat, W. Xu, G. Xiao, C. Qin, Z. Shi, H. Jiang, Z. Rao and H. Yang (2020). "Structure of M(pro) from SARS-CoV-2 and discovery of its inhibitors." Nature 582(7811): 289-293.

Kandeel, M., A. H. M. Abdelrahman, K. Oh-Hashi, A. Ibrahim, K. N. Venugopala, M. A. Morsy and M. A. A. Ibrahim (2021). "Repurposing of FDA-approved antivirals, antibiotics, anthelmintics, antioxidants, and cell protectives against SARS-CoV-2 papain-like protease." Journal of Biomolecular Structure and Dynamics 39(14): 5129-5136.

Kaur, S. P. and V. Gupta (2020). "COVID-19 Vaccine: A comprehensive status report." Virus Res 288: 198114.

Kim, D., J.-Y. Lee, J.-S. Yang, J. W. Kim, V. N. Kim and H. Chang (2020). "The Architecture of SARS-CoV-2 Transcriptome." Cell 181(4): 914-921.e910.

Klemm, T., G. Ebert, D. J. Calleja, C. C. Allison, L. W. Richardson, J. P. Bernardini, B. G. Lu, N. W. Kuchel, C. Grohmann, Y. Shibata, Z. Y. Gan, J. P. Cooney, M. Doerflinger, A. E. Au, T. R. Blackmore, G. J. van der Heden van Noort, P. P. Geurink, H. Ovaa, J. Newman, A. Riboldi-Tunnicliffe, P. E. Czabotar, J. P. Mitchell, R. Feltham, B. C. Lechtenberg, K. N. Lowes, G. Dewson, M. Pellegrini, G. Lessene and D. Komander (2020). "Mechanism and inhibition of the papain-like protease, PLpro, of SARS-CoV-2." Embo j 39(18): e106275.

Krichel, B., S. Falke, R. Hilgenfeld, L. Redecke and C. Uetrecht (2020). "Processing of the SARS-CoV pp1a/ab nsp7-10 region." Biochem J 477(5): 1009-1019.

Krishna SS, Majumdar I, Grishin NV. Structural classification of zinc fingers: survey and summary. Nucleic Acids Res. 2003 Jan 15;31(2):532-50. doi: 10.1093/nar/gkg161. PMID: 12527760; PMCID: PMC140525.

Lan, F. Y., R. Filler, S. Mathew, J. Buley, E. Iliaki, L. A. Bruno-Murtha, R. Osgood, C. A. Christophi, A. Fernandez-Montero and S. N. Kales (2020). "COVID-19 symptoms predictive of healthcare workers' SARS-CoV-2 PCR results." PLoS One 15(6): e0235460.

Li, F. (2016). "Structure, Function, and Evolution of Coronavirus Spike Proteins." Annu Rev Virol 3(1): 237-261.

Lim, C. T., K. W. Tan, M. Wu, R. Ulferts, L. A. Armstrong, E. Ozono, L. S. Drury, J. C. Milligan, T. U. Zeisner, J. Zeng, F. Weissmann, B. Canal, G. Bineva-Todd, M. Howell, N. O'Reilly, R. Beale, Y. Kulathu, K. Labib and J. F. X. Diffley (2021). "Identifying SARS-CoV-2 antiviral compounds by screening for small molecule inhibitors of Nsp3 papain-like protease." Biochemical Journal 478(13): 2517-2531.

Lin, M. H., D. C. Moses, C. H. Hsieh, S. C. Cheng, Y. H. Chen, C. Y. Sun and C. Y. Chou (2018). "Disulfiram can inhibit MERS and SARS coronavirus papain-like proteases via different modes." Antiviral Res 150: 155-163.

Luo, L., Q. Qiu, F. Huang, K. Liu, Y. Lan, X. Li, Y. Huang, L. Cui and H. Luo (2021). "Drug repurposing against coronavirus disease 2019 (COVID-19): A review." Journal of Pharmaceutical Analysis 11(6): 683-690.

Lv, Z., K. E. Cano, L. Jia, M. Drag, T. T. Huang and S. K. Olsen (2021). "Targeting SARS-CoV-2 Proteases for COVID-19 Antiviral Development." Front Chem 9: 819165.

Ma, C., Y. Hu, J. A. Townsend, P. I. Lagarias, M. T. Marty, A. Kolocouris and J. Wang (2020). "Ebselen, Disulfiram, Carmofur, PX-12, Tideglusib, and Shikonin Are Nonspecific Promiscuous SARS-CoV-2 Main Protease Inhibitors." ACS Pharmacol Transl Sci. 3(6): 1265-1277.

Ma, C., M. D. Sacco, Z. Xia, G. Lambrinidis, J. A. Townsend, Y. Hu, X. Meng, T. Szeto, M. Ba, X. Zhang, M. Gongora, F. Zhang, M. T. Marty, Y. Xiang, A. Kolocouris, Y. Chen and J. Wang (2021). "Discovery of SARS-CoV-2 Papain-like Protease Inhibitors through a Combination of High-Throughput Screening and a FlipGFP-Based Reporter Assay." ACS Cent Sci 7(7): 1245-1260.

McClain, C. B. and N. Vabret (2020). "SARS-CoV-2: the many pros of targeting PLpro." Signal Transduction and Targeted Therapy 5(1): 223.

Maestro, Schrödinger, LLC, New York, NY, 2021. Available from: Http://Www.Schrodinger.Com/.

Molecular Operating Environment (MOE), 2019.01; Chemical Computing Group ULC, 1010 Sherbooke St. West, Suite #910, Montreal, QC, Canada, H3A 2R7, 2021.

Mura, C., S. Preissner, R. Preissner and P. E. Bourne (2021). "A Birds-Eye (Re)View of Acid-Suppression Drugs, COVID-19, and the Highly Variable Literature." Front Pharmacol 12: 700703.

Osipiuk, J., S. A. Azizi, S. Dvorkin, M. Endres, R. Jedrzejczak, K. A. Jones, S. Kang, R. S. Kathayat, Y. Kim, V. G. Lisnyak, S. L. Maki, V. Nicolaescu, C. A. Taylor, C. Tesar, Y. A. Zhang, Z. Zhou, G. Randall, K. Michalska, S. A. Snyder, B. C. Dickinson and A. Joachimiak (2021). "Structure of papain-like protease from SARS-CoV-2 and its complexes with non-covalent inhibitors." Nat Commun 12(1): 743.

Protein Preparation Wizard; Epik, Schrödinger, LLC, New York, NY, 2021; Impact, Schrödinger, LLC, New York, NY; Prime, Schrödinger, LLC, New York, NY, 2021. Available from: Http://Www.Schrodinger.Com/.

Pushpakom, S., F. Iorio, P. A. Eyers, K. J. Escott, S. Hopper, A. Wells, A. Doig, T. Guilliams, J. Latimer, C. McNamee, A. Norris, P. Sanseau, D. Cavalla and M. Pirmohamed (2019). "Drug repurposing: progress, challenges and recommendations." Nature Reviews Drug Discovery 18(1): 41-58.

Quimque, M. T. J., K. I. R. Notarte, R. A. T. Fernandez, M. A. O. Mendoza, R. A. D. Liman, J. A. K. Lim, L. A. E. Pilapil, J. K. H. Ong, A. M. Pastrana, A. Khan, D. Q. Wei and A. P. G. Macabeo (2021). "Virtual screening-driven drug discovery of SARS-CoV2 enzyme inhibitors targeting viral attachment, replication, post-translational modification and host immunity evasion infection mechanisms." J Biomol Struct Dyn 39(12): 4316-4333.

Raj, R. (2021). "Analysis of non-structural proteins, NSPs of SARS-CoV-2 as targets for computational drug designing." Biochem Biophys Rep 25: 100847.

Ratia, K., A. Kilianski, Y. M. Baez-Santos, S. C. Baker and A. Mesecar (2014). "Structural Basis for the Ubiquitin-Linkage Specificity and deISGylating activity of SARS-CoV papain-like protease." PLoS Pathog 10(5): e1004113.

Redhead, M. A., C. D. Owen, L. Brewitz, A. H. Collette, P. Lukacik, C. Strain-Damerell, S. W. Robinson, P. M. Collins, P. Schäfer, M. Swindells, C. J. Radoux, I. N. Hopkins, D. Fearon, A. Douangamath, F. von Delft, T. R. Malla, L. Vangeel, T. Vercruysse, J. Thibaut, P. Leyssen, T.-T. Nguyen, M. Hull, A. Tumber, D. J. Hallett, C. J. Schofield, D. I. Stuart, A. L. Hopkins and M. A. Walsh (2021). "Bispecific repurposed medicines targeting the viral and immunological arms of COVID-19." Scientific Reports 11(1): 13208.

Rohaim, M. A., R. F. El Naggar, E. Clayton and M. Munir (2021). "Structural and functional insights into non-structural proteins of coronaviruses." Microb Pathog 150: 104641.

Sargsyan, K., C.-C. Lin, T. Chen, C. Grauffel, Y.-P. Chen, W.-Z. Yang, H. S. Yuan and C. Lim (2020). "Multi-targeting of functional cysteines in multiple conserved SARS-CoV-2 domains by clinically safe Zn-ejectors." Chemical Science 11(36): 9904-9909.

Shan, H., J. Liu, J. Shen, J. Dai, G. Xu, K. Lu, C. Han, Y. Wang, X. Xu, Y. Tong, H. Xiang, Z. Ai, G. Zhuang, J. Hu, Z. Zhang, Y. Li, L. Pan and L. Tan (2021). "Development of potent and selective inhibitors targeting the papain-like protease of SARS-CoV-2." Cell Chem Biol 28(6): 855-865.e859.

Shetler, C. L., J. C. Ferreira, T. H. S. Cardoso, E. M. A. Silva, N. K. Saksena and W. M. Rabeh (2022). "Therapeutic potential of metal ions for COVID-19: insights from the papain-like protease of SARS-CoV-2." Biochem J 479(20): 2175-2193.

Shiwani Rana, M. P. a. K. S. G. (2021). "Docking Studies with Multiple Molecular Targets Associated with SARSCoV-2 for Drug Repurposing." Coronaviruses 2(8).

SiteMap, Schrödinger, LLC, New York, NY, 2021. Available from: Http://Www.Schrodinger.Com/.

Smith, E., M. E. Davis-Gardner, R. D. Garcia-Ordonez, T. T. Nguyen, M. Hull, E. Chen, P. Baillargeon, L. Scampavia, T. Strutzenberg, P. R. Griffin, M. Farzan and T. P. Spicer (2020). "High-Throughput Screening for Drugs That Inhibit Papain-Like Protease in SARS-CoV-2." SLAS Discov 25(10): 1152-1161.

V'Kovski, P., A. Kratzel, S. Steiner, H. Stalder and V. Thiel (2021). "Coronavirus biology and replication: implications for SARS-CoV-2." Nat Rev Microbiol 19(3): 155-170.

Weglarz-Tomczak, E., J. M. Tomczak, M. Talma, M. Burda-Grabowska, M. Giurg and S. Brul (2021). "Identification of ebselen and its analogues as potent covalent inhibitors of papain-like protease from SARS-CoV-2." Sci Rep 11(1): 3640.

WHO. (2022). "World Health Organization Coronavirus (COVID-19) Dashboard." Retrieved February 13, 2023, 2022, from https://covid19.who.int/.

Wu, D., T. Wu, Q. Liu and Z. Yang (2020). "The SARS-CoV-2 outbreak: What we know." Int J Infect Dis 94: 44-48.

Wu, Y. C., C. S. Chen and Y. J. Chan (2020). "The outbreak of COVID-19: An overview." J Chin Med Assoc 83(3): 217-220.

Xu, Y., K. Chen, J. Pan, Y. Lei, D. Zhang, L. Fang, J. Tang, X. Chen, Y. Ma, Y. Zheng, B. Zhang, Y. Zhou, J. Zhan and W. Xu (2021). "Repurposing clinically approved drugs for COVID-19 treatment targeting SARS-CoV-2 papain-like protease." International Journal of Biological Macromolecules 188: 137-146.

Yang, X., X. Chen, G. Bian, J. Tu, Y. Xing, Y. Wang and Z. Chen (2014). "Proteolytic processing, deubiquitinase and interferon antagonist activities of Middle East respiratory syndrome coronavirus papain-like protease." J Gen Virol. 95(3): 614-626.

Zhang, Q., R. Xiang, S. Huo, Y. Zhou, S. Jiang, Q. Wang and F. Yu (2021). "Molecular mechanism of interaction between SARS-CoV-2 and host cells and interventional therapy." Signal Transduct Target Ther 6(1): 233.

Zhao, Y., X. Du, Y. Duan, X. Pan, Y. Sun, T. You, L. Han, Z. Jin, W. Shang, J. Yu, H. Guo, Q. Liu, Y. Wu, C. Peng, J. Wang, C. Zhu, X. Yang, K. Yang, Y. Lei, L. W. Guddat, W. Xu, G. Xiao, L. Sun, L. Zhang, Z. Rao and H. Yang (2021). "High-throughput screening identifies established drugs as SARS-CoV-2 PLpro inhibitors." Protein & Cell 12(11): 877-888.

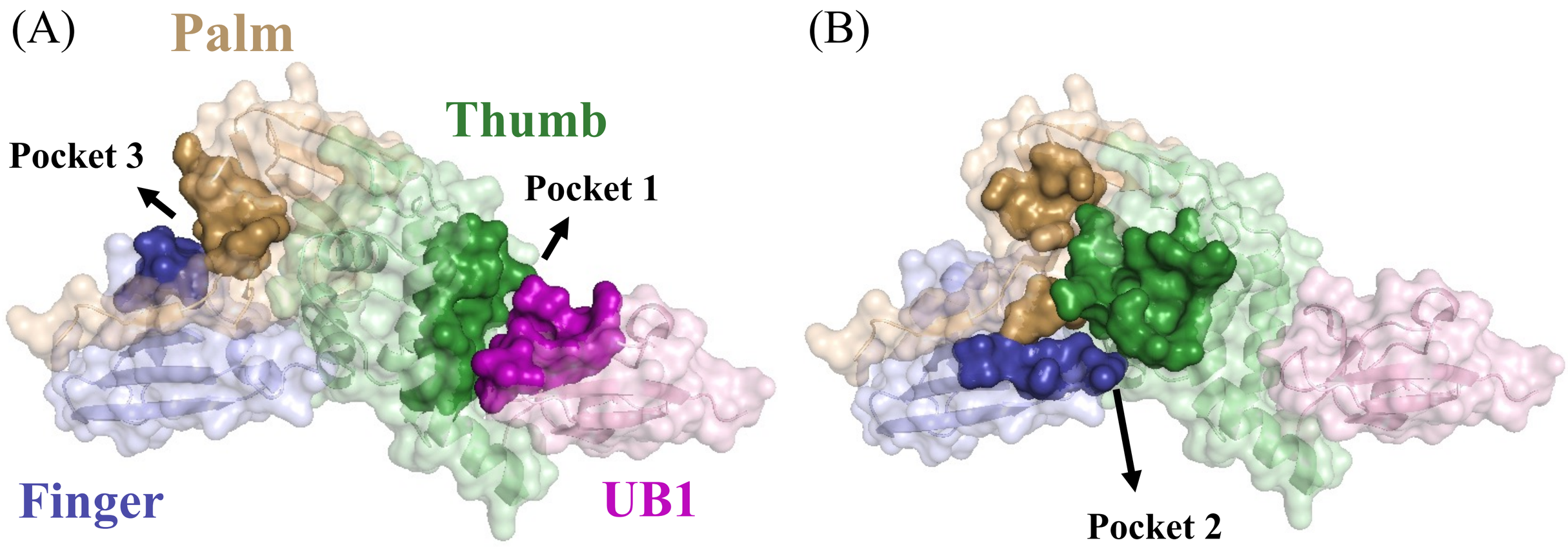

Figure 1. Surface Representation of the PLpro protease and the computationally-predicted PLpro pockets. (A) Location of Pocket 1 (cleft between Thumb and UB1) and Pocket 3 (cleft between Palm and Finger). Each PLpro domain is colored accordingly: Finger domain is blue, Palm domain is beige, Thumb domain is green, and UB1 domain is pink. **(B)** Location of pocket 2 (cavity formed between Palm, Finger, and Thumb).

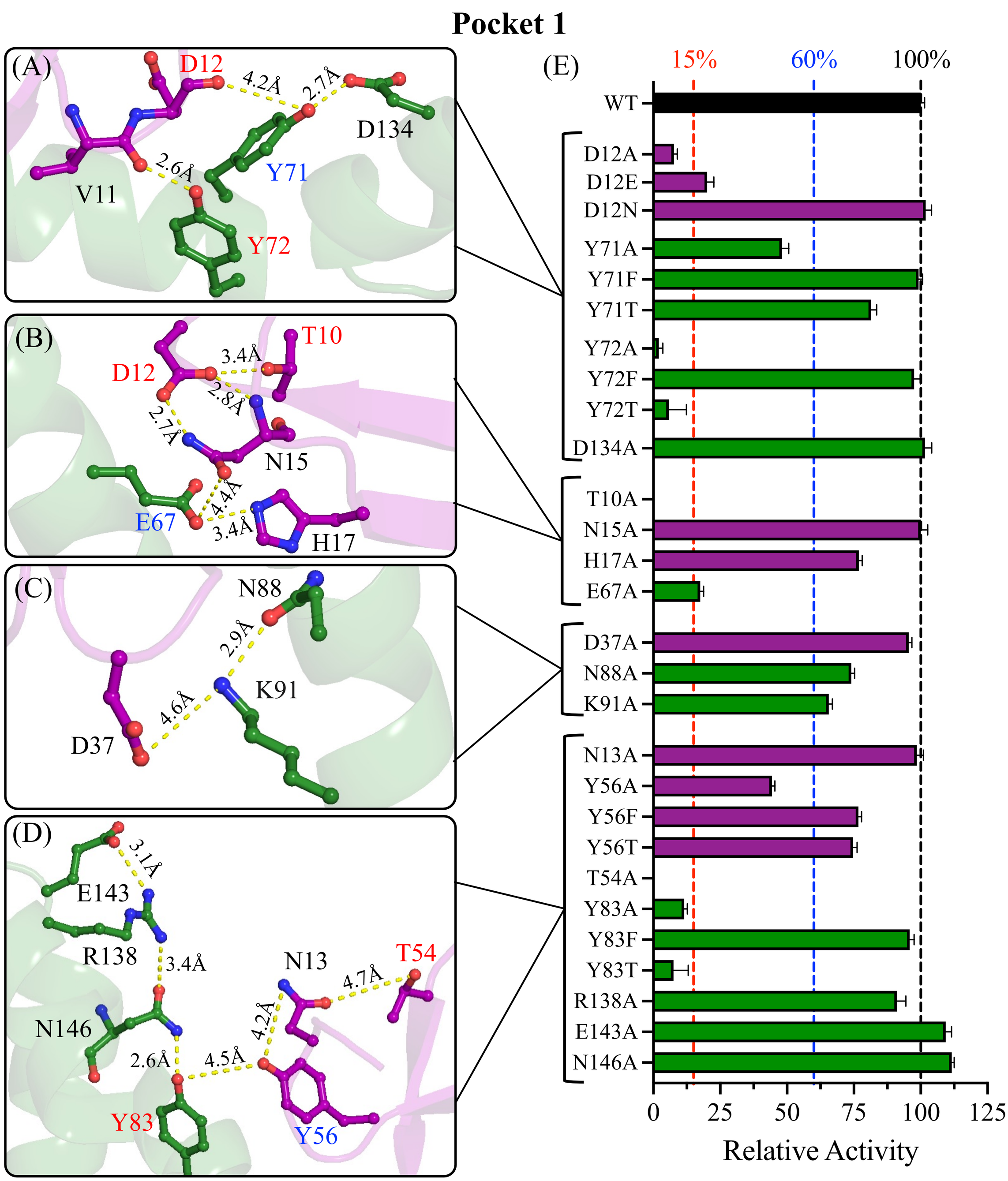

Figure 2. Key residues at the computationally-predicted allosteric site, Pocket 1, of SARS-CoV-2 PLpro and their implications on proteolysis upon site-directed mutagenesis. The amino acids represented here are located at Pocket 1. The colors of the amino acids correspond to the domain colors established in Fig. 1. Amino acids presented above were mutated to alanine and were assessed for their proteolytic function. (**A-D**) Polar interactions formed by amino acids in pocket 1. Amino acid labels are color coded based on their effects on proteolysis upon site-directed mutagenesis: Red (<15% proteolytic activity), Blue (<60% and >15% proteolytic activity) and Black (minimal or no effect in proteolytic activity). Partial inactivation in proteolytic activity was defined to be less than 60% of proteolytic activity relative to that of WT. **(E)** Effect of the alanine substitutions in pocket 1 on the catalytic activity of PLpro. Mutant proteolytic activities were normalized against the proteolytic activity of WT. Proteolytic activities were obtained from an enzyme titration assay at a fixed substrate concentration (200 μM) and varying enzyme concentrations (0.5 - 5.0 μM). Color of the bar plot correspond to the domain the amino acid residue belongs to (Blue = Finger, Beige = Palm, Green = Thumb, and Pink = UB1). The data are presented as mean ± SD, n=3.

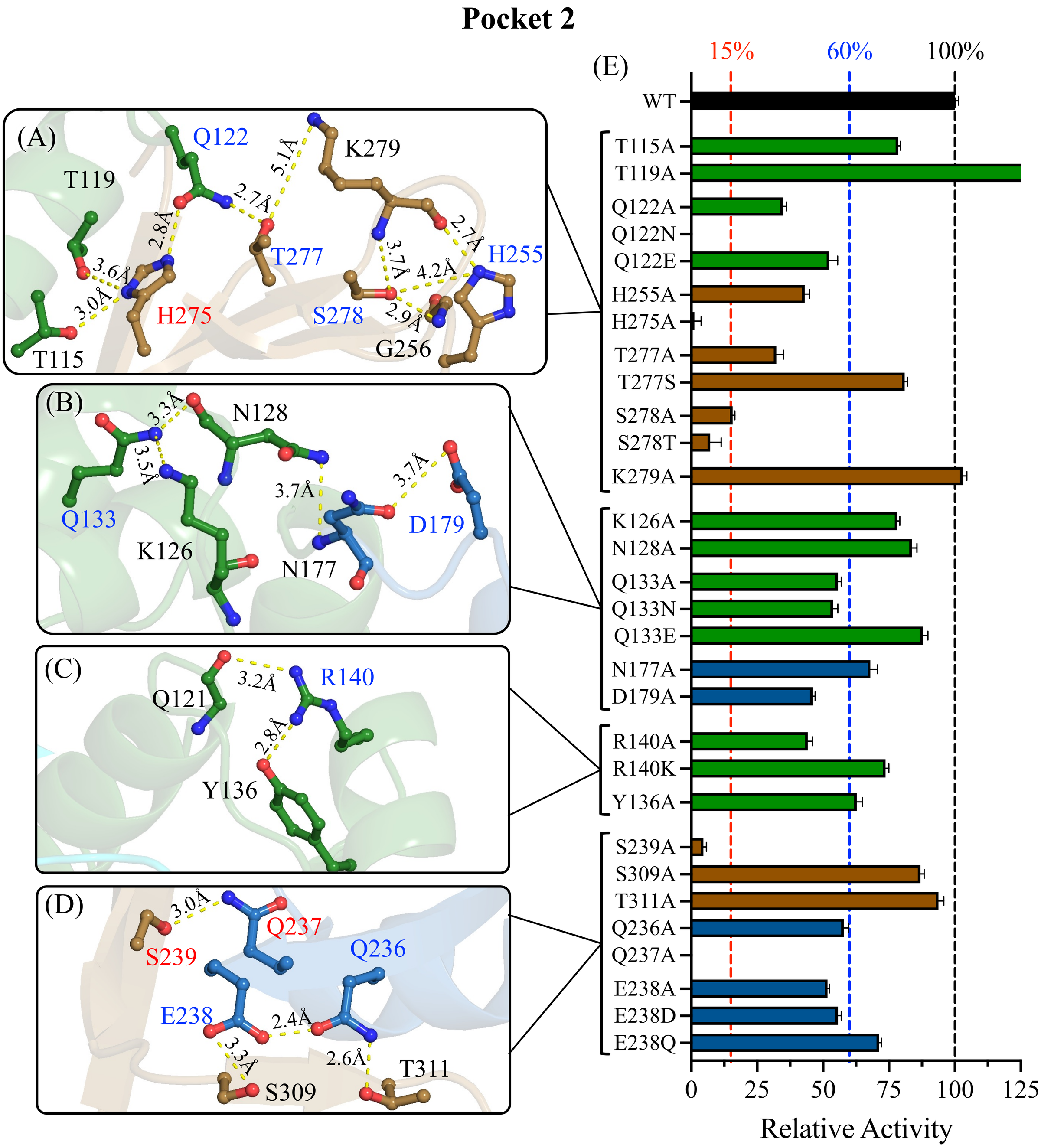

Figure 3. Key residues at the computationally-predicted allosteric site, Pocket 2, of SARS-CoV-2 PLpro and their implications on proteolysis upon site-directed mutagenesis. The amino acids represented here are located at Pocket 2, a cavity formed between Thumb, Finger and Palm. The colors of the amino acids correspond to the domain colors established in Fig. 1. Amino acids presented above were mutated to alanine and were assessed for their proteolytic function. (**A-D)** Polar interactions formed by amino acids in pocket 2. Amino acid labels are color coded based on their effects on proteolysis upon site-directed mutagenesis: Red (<15% proteolytic activity), Blue (<60% and >15% proteolytic activity) and Black (minimal or no effect in proteolytic activity). Partial inactivation in proteolytic activity was defined to be less than 60% of proteolytic activity relative to that of WT. **(E)** Effect of the alanine substitutions in pocket 2 on the catalytic activity of PLpro. Mutant proteolytic activities were normalized against the proteolytic activity of WT. Proteolytic activities were obtained from an enzyme titration assay at a fixed substrate concentration (200 μM) and varied enzyme concentrations (0.5 - 5.0 μM). Color of the bar plot correspond to the domain the amino acid residue belongs to (Blue = Finger, Beige = Palm, Green = Thumb, and Pink = UB1). The data are presented as mean ± SD, n=3.

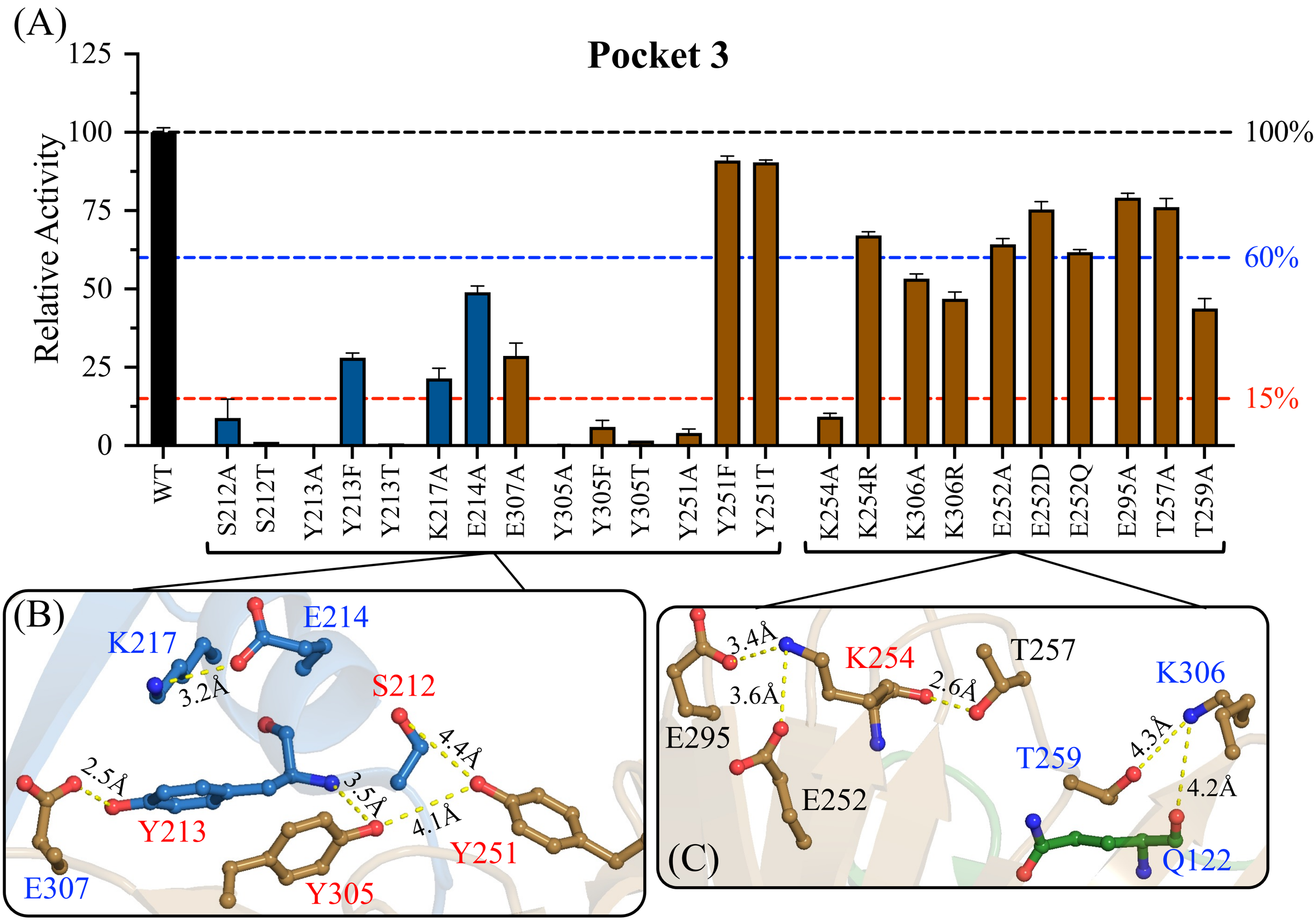

Figure 4. Key residues at the computationally-predicted allosteric site, Pocket 3, of SARS-CoV-2 PLpro and their implications on proteolysis upon site-directed mutagenesis. The amino acids represented here are located at Pocket 3, a cavity formed between Finger and Palm. The colors of the amino acids correspond to the domain colors established in Fig. 1. Amino acids presented above were mutated to alanine and were assessed for their proteolytic function. **(A-D)** Polar interactions formed by amino acids in pocket 3. Amino acid labels are color coded based on their effects on proteolysis upon site-directed mutagenesis: Red (<15% proteolytic activity), Blue (<60% and >15% proteolytic activity) and Black (minimal or no effect in proteolytic activity). Partial inactivation in proteolytic activity was defined to be less than 60% of proteolytic activity relative to that of WT. **(E)** Effect of the alanine substitutions in pocket 2 on the catalytic activity of PLpro. Mutant proteolytic activities were normalized against the proteolytic activity of WT. Proteolytic activities were obtained from an enzyme titration assay at a fixed substrate concentration (200 μM) and varied enzyme concentrations (0.5 - 5.0 μM). Color of the bar plot correspond to the domain the amino acid residue belongs to (Blue = Finger, Beige = Palm, Green = Thumb, and Pink = UB1). The data are presented as mean ± SD, n=3.

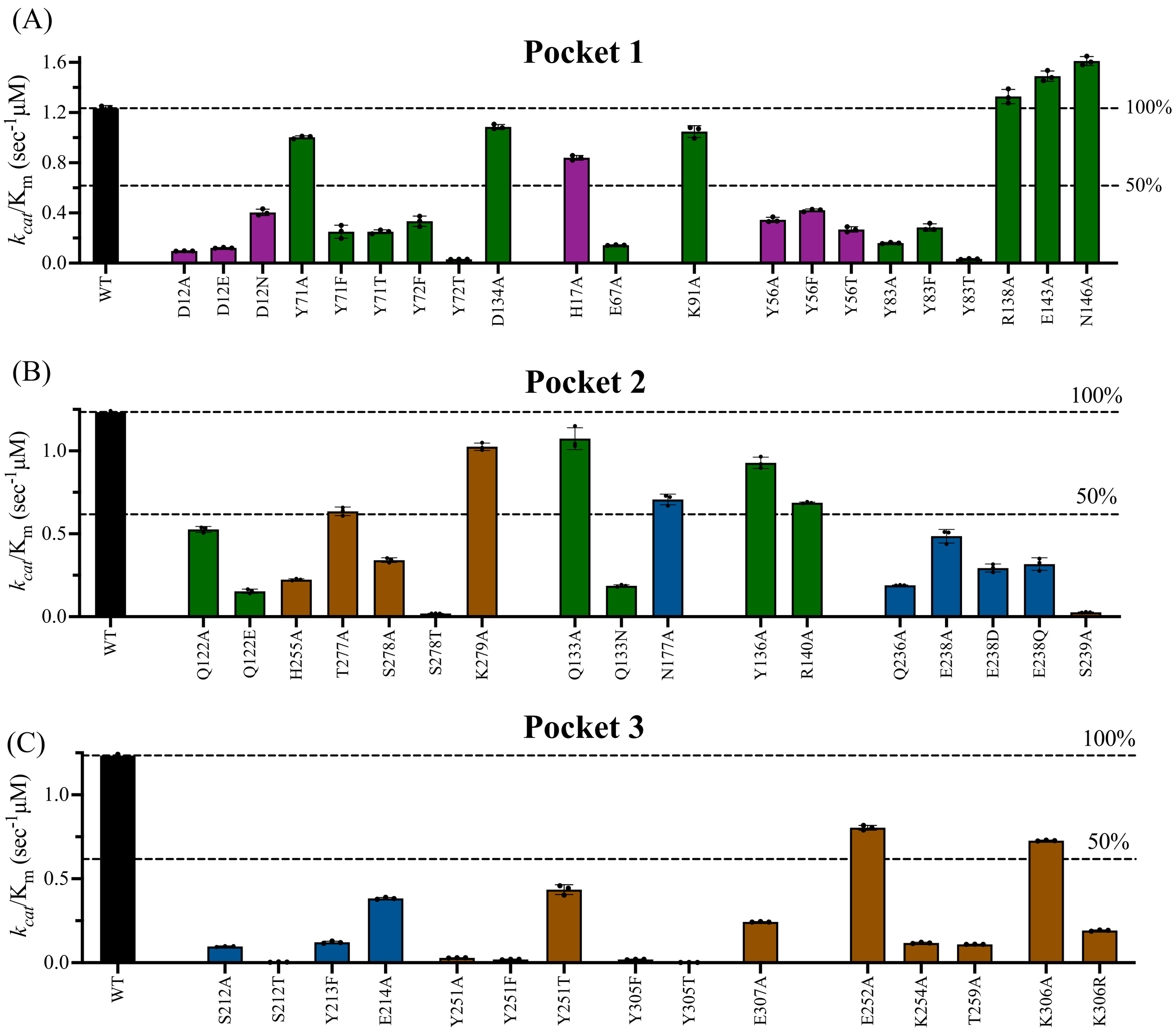

Figure 5: Kinetic characterization of the enzymatically active PLpro mutants. Recovery mutants and alanine mutants (<60% Relative enzymatic activity) were investigated further with kinetic studies**.** Bar plots of catalytic efficiencies of WT PLpro (black bars), **(A)** Pocket 1 mutants, **(B)** Pocket 2 mutants, and **(C)** Pocket 3 mutants. Color of the bar plot correspond to the domain the amino acid residue belongs to (Blue = Finger, Beige = Palm, Green = Tumb, and Pink = UB1). The initial velocity rates were measured at 25 °C and in the in buffer containing 20 mM HEPES, pH 7.5, 100 mM NaCl, 1 mM EDTA, 1 mM TCEP. The data points represent the mean ± SD of triplicate measurements.

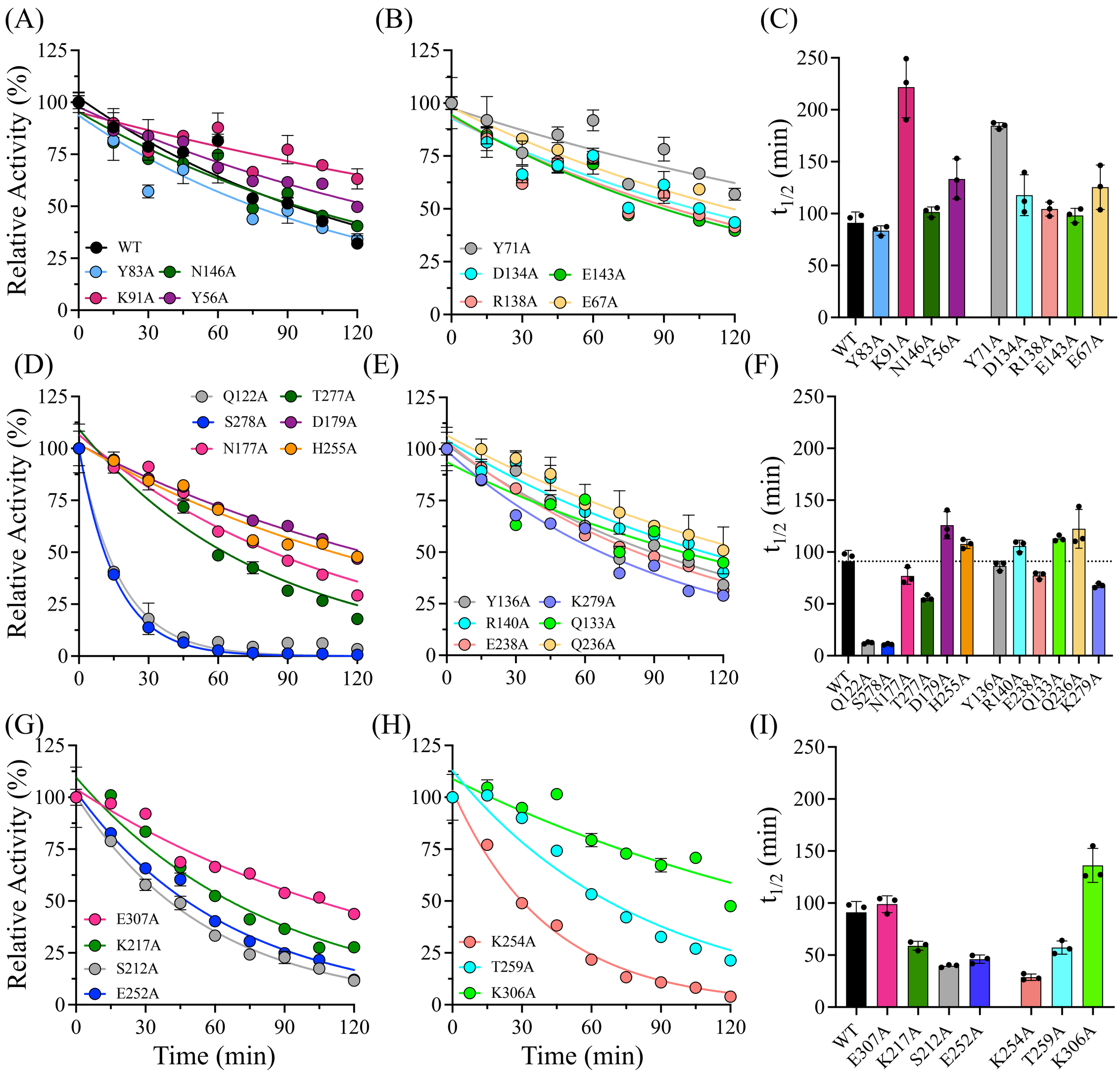

Figure 6. Calculation of Half-life ($t_{1/2}$) In 15-minute time intervals, the remaining enzymatic activity of each PLpro variant was measured while incubating the enzyme at 37 °C for two hours. **(A-C)** Pocket 1. **(D-F)** Pocket 2. **(G-I)** Pocket 3. Data are presented as mean ± S.D., n=3.